Engineering Seismology Group Canada Report ESG98-11

REPORT

TO

GAS RESEARCH INSTITUTE

ON

COTTON VALLEY HYDRAULIC FRACTURE IMAGING PROJECT: PHASE II (CGU21-9) FRACTURE IMAGING USING MICROSEISMIC EVENT LOCATIONS

JUNE, 1998

Ted Urbancic

1.0 Introduction

Hydraulic fracturing is widely used to stimulate production in oil and gas fields throughout the U.S.. However, currently no method exists that can provide well operators with information on fracture dimensions in real time. The Cotton Valley Hydraulic Fracture Imaging Project, as initiated by a consortium of companies (UPR, Texaco, Amoco, Arco, Chevron), was established to determine if the monitoring of microseismicity was feasible, if microseismicity can remotely provide accurate measurements of fracture geometry (azimuth, height, length, width, asymmetry) and growth, and if recording / analysis procedures can eventually be implemented to allow for real time monitoring (Walker, 1997). The presence of microseismicity was confirmed during the Phase I treatment of well CGU 22-10 in May, 1997 (see Figure 1 for layout). The analysis for fracture dimensions involved the testing of various location techniques (forward modeling and inversion schemes) by ARCO, ESG, Los Alamos, and Sandia National Labs. To locate events, ARCO employed a series of model curves derived from pre-fracture shots in the treatment well and visual curve matching for data recorded in both monitoring wells. ESG examined inversion approaches that could potentially result in the real-time determination of event locations and source parameters (characteristics of source size, strength, energy and stress release). The ESG analyses concluded that it is possible to use automatically determined P- and S-wave arrivals for a subset of signals recorded in the two monitoring wells, direction vectors (hodograms), and the inclusion of velocity variations to effectively locate events to an accuracy on average better than 50 ft. (Urbancic, 1998). Both Los Alamos and Sandia considered the effect of array decimation on location which resulted in varying degrees of success.

A Phase II was implemented in July, 1997, with the fracturing of well CGU21-9. The treatment took place over three days (July 14, 16, and 18) and was supplemented with perforation shots on July 17. Although signals were recorded from sensors located in three wells (triaxial geophones in wells CGU21-9 and CGU22-9, 48 hydrophones in CGU22-7), only the array in well CGU22-9 provided interpretable data. In their analysis of the Phase II data, Withers and Dart (1997) were able to locate 164 events of 1,826 detected events by incorporating directionality into their forward modelling approach. The small number of located events was primarily a result of generally weaker signals as compared to those recorded during Phase I, and the large percentage of events that were deficient in P-wave energy, making analysis by their technique difficult. As shown in Figure 2, the derived locations were scattered and markedly different from the expected trend of N70E, raising questions as to whether the technique employed was appropriate or whether the geometrical constraints imposed by single-well monitoring limits does not allow for events to be located to any degree of accuracy.

The purpose of this study is to re-evaluate the 164 event locations reported by Withers and Dart in order to provide an independent assessment of the Phase II data. An initial determination of triaxial geophone alignment is made based on hodogram (particle motion diagram) analysis of known sources (primacord shots from Phase I, and two Phase II perforation shots). Further, a maximum likelihood inverse approach based on P- and S- wave arrival times,

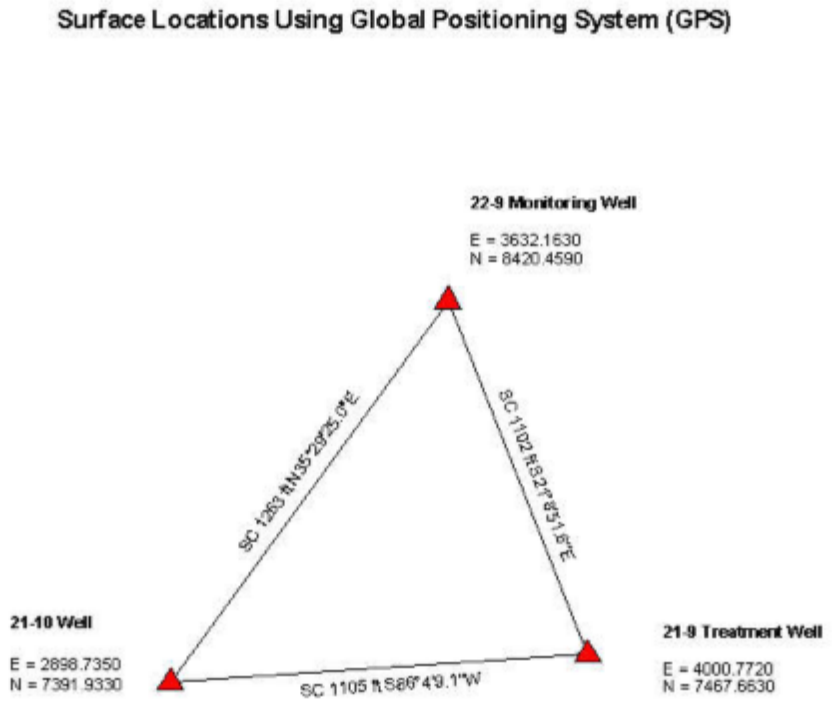

Figure 1. Surface layout of the treatment and monitoring wells employed during the Phase II hydraulic fracture experiments. During Phase I, the treatment well was 21-10 and both 21-9 and 22-9 were the monitoring wells. The indicated coordinates were employed in this study and all measurements are in feet.

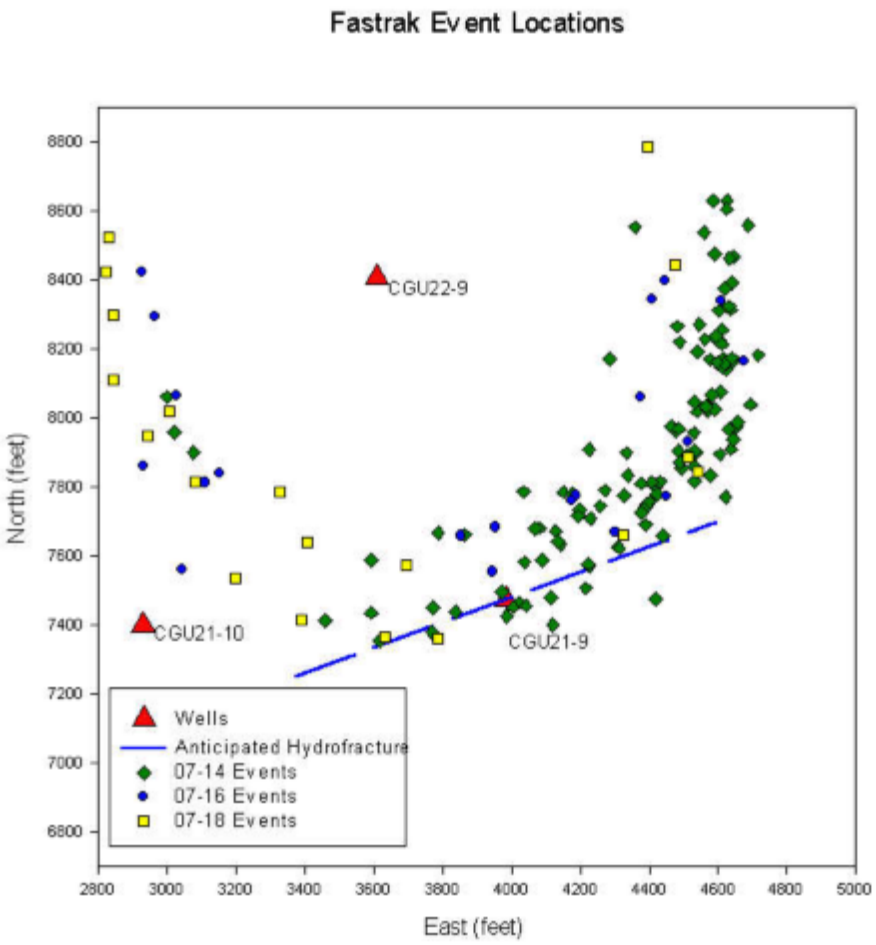

Figure 2. Locations of events determined using the forward modeling Fastrak approach as reported by Withers and Dart (1997). The anticipated hydrofracture orientation is based on the observed distribution of events during Phase I and numerically predicted.

and both P- and S-wave polarization angles is employed to obtain event locations. Location errors for the derived locations are also provided in order to assess location reliability. The probability of on-line analysis based on single-well recordings is also briefly discussed.

2.0 Receiver Characteristics

As outlined, studies by Los Alamos and Sandia National Laboratories (Rutledge et al., 1998; Warpinski, 1997), a level of uncertainty exists in the rotoscan-derived receiver orientations. To remove this uncertainty, hodgrams were evaluated for known shot locations in order to obtain corrected sensor orientations. Here, rather than relying on actual particle-motion diagrams, we mathematically fit the particle motion to an ellipsoid. The major axis of that ellipsoid is then aligned to the direction back to the source. With the layered nature of the geology, the plunge angle to the receiver may be affected, but the azimuth should be reasonable as there is little reason to suspect large lateral variations in seismic velocity. The sensor orientation was then corrected by the difference between the known azimuth to the source, and the derived raypath orientation. The results were subsequently applied to all microseismic hodogram data.

In this analysis, this method was applied to each triaxial geophone station with at least two working horizontal components in well CGU22-9 (Figure 3). The sensor orientations were corrected using the average orientation determined from five shots at similar depths to the sensor being tested. The standard deviations for the orientations generally ranged from about 2 to 3 degrees. The corrected orientations differed up to a maximum of 18 degrees from the rotoscan derived orientations. In Table 1, the azimuth of the H2 component of each sensor is given. The H1 component is 90 degrees clockwise of H2 and the vertical component was taken as down. Triaxial stations 16 and 19 were considered to be cross wired, and were therefore not used.

3.0 Data Processing

In this study, source locations were determined based on a two-stage approach using P and S-wave arrival times, and particle-motion direction vectors. The first step involved defining a two-dimensional plane corresponding to the azimuth determined from the overall particle motions for the sensor array. This was followed by a performing a 2-D travel-time inversion within that plane in order to obtain the location..

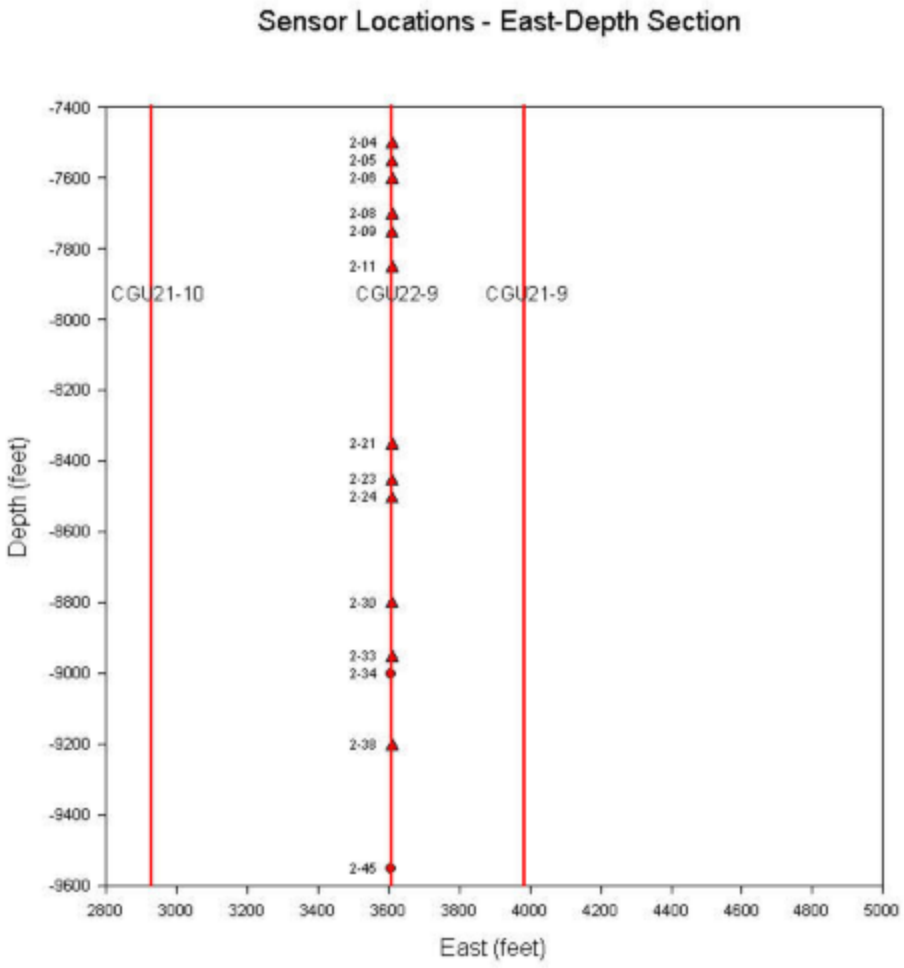

Figure 3. Sensor array in CGU22-9 employed in Phase II data re-analysis. Sensors with three functioning components are depicted by triangles, whereas triaxial sensors with less than three operational components are presented as filled circles.

Station	H2 Azimuth
4	257
5	253
6	259
8	249
9	282
11	281
12	273
13	256
20	258
21	258
23	250
24	244
30	232
33	268
34	231
38	245

Table 1. Orientation of H2 component of the triaxial sensors from well CGU22-9 used for event locations.

As previously discussed, the data quality was quite variable, and in many instances the P-wave amplitudes were often lost within the background noise. P-wave arrival times were often only evident on stations 21 and below. The S-wave arrival times, however, were generally quite strong and could be picked on most stations. In our analysis, we attempted to window the first P-wave motion on at least three triaxial stations to obtain particle-motion estimates of the azimuth back to the source. In some cases this was not possible. In these cases, a method was developed to estimate the receiver to source direction based on the first S-wave motion, which were found to be strongly horizontally polarised. Testing on events with both strong P-wave and S-wave amplitudes indicated that the S-wave particle motion was within a couple degrees of being perpendicular to the P-wave particle motion, and therefore the normal to the horizontal S-wave polarization direction at the receiver could be taken as a good estimate of the azimuth back to the source. P-wave and S-wave arrival times were also picked on some deeper stations with malfunctioning components, however, no particle motion polarization information was used from these stations.

After determining the azimuth based predominantly P-wave particle motion and in a few cases S-wave particle motion, the single well solution was treated as a two dimensional case. The General 2D Method is based on a simple equation for the P wave arrival time in an isotropic homogeneous medium

$$t_P = t_o + \frac{\sqrt{R^2 + (h_i - h_{source})^2}}{V_P}$$

This equation has three unknowns, the source time t_0, the source depth h_{source} and the radial distance R of the event. Solving for the three unknowns follows an iterative, non-linear least-squares method which involves minimizing the following equation with respect to t_0, h_{source} and R.

$$\sum_{i=1}^{n}\left[t_{Pi} - t_o - \frac{\sqrt{R^2 + (h_i - h_{source})^2}}{V_P} \right]^2$$

Similar equations are defined for the S wave travel times. The least-squares algorithm is based on the Levenberg-Marquardt method, which is a weighted average of the inverse-Hessian method and the Steepest Descent method. Initially, the Steepest Descent method is weighted heavier than the inverse-Hessian method, however, once convergence is detected, the weighting is shifted towards the more rapidly convergent inverse-Hessian method (Press et al., 1992).

4.0 Results

A total of 550, 311 and 975 events were detected during the three fracture stages (07-14-1997, 07-16-1997, 07-18-1997), respectively. Of these, Withers and Dart (1997) determined event locations for 120, 21 and 23 relatively high quality (large signal to noise) events using their Fastrak method. Of the Fastrak-located events, we were able to locate 116, 20 and 23 events, respectively. The handful of Fastrak events not located was due to access errors in attempting to read the SEGY data files rather than any difficulty in processing the events.

Figures 4-6 shows different views of all the located events from the three stages. The dashed line indicates the expected position of the fractures based on the N70°E fracture direction observed during Phase I. Generally, the events form a linear feature, which appears to be shifted somewhat to the north (toward the observation well) from the anticipated position. Based on a linear regression analysis of these data, the trend of the feature defined by the events is N75°E. In Figure 7, the depth of the events are compared to the perforation depths (delimited by pairs of dashed lines) in the treatment well. Overall, there is a good correlation to the perforation depths for most events.

To assess the relaibility of the observed trends, location errors were determined for the events as shown in Figures 8 and 9. In Figure 8, vectorial standard deviations are shown along with the errors in Easting, Northing and Depth. These errors are statistical and as such do not fully account for any systematic shift in the data. In general, using the current single well array geometry, the uncertainty in location can be considered to be about +/- 150 ft., with the largest errors in the easting and northing components (around +/- 100 ft.; see 0714). As seen in Figure 9, there is a slight tendency for the errors to increase towards the south and to the west of the treatment well, however, the observed distribution trends in event location generally remain unaffected.

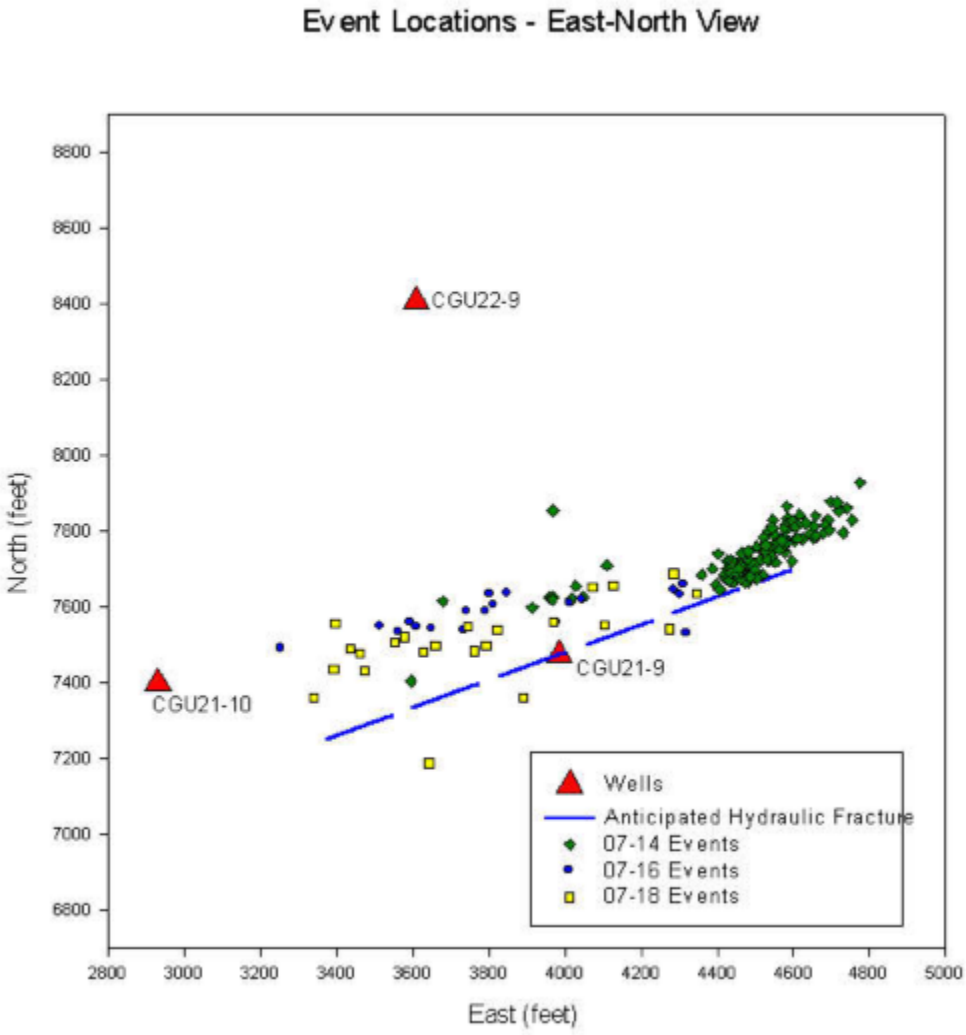

Figure 4. Plan view of seismicity located during Phase II

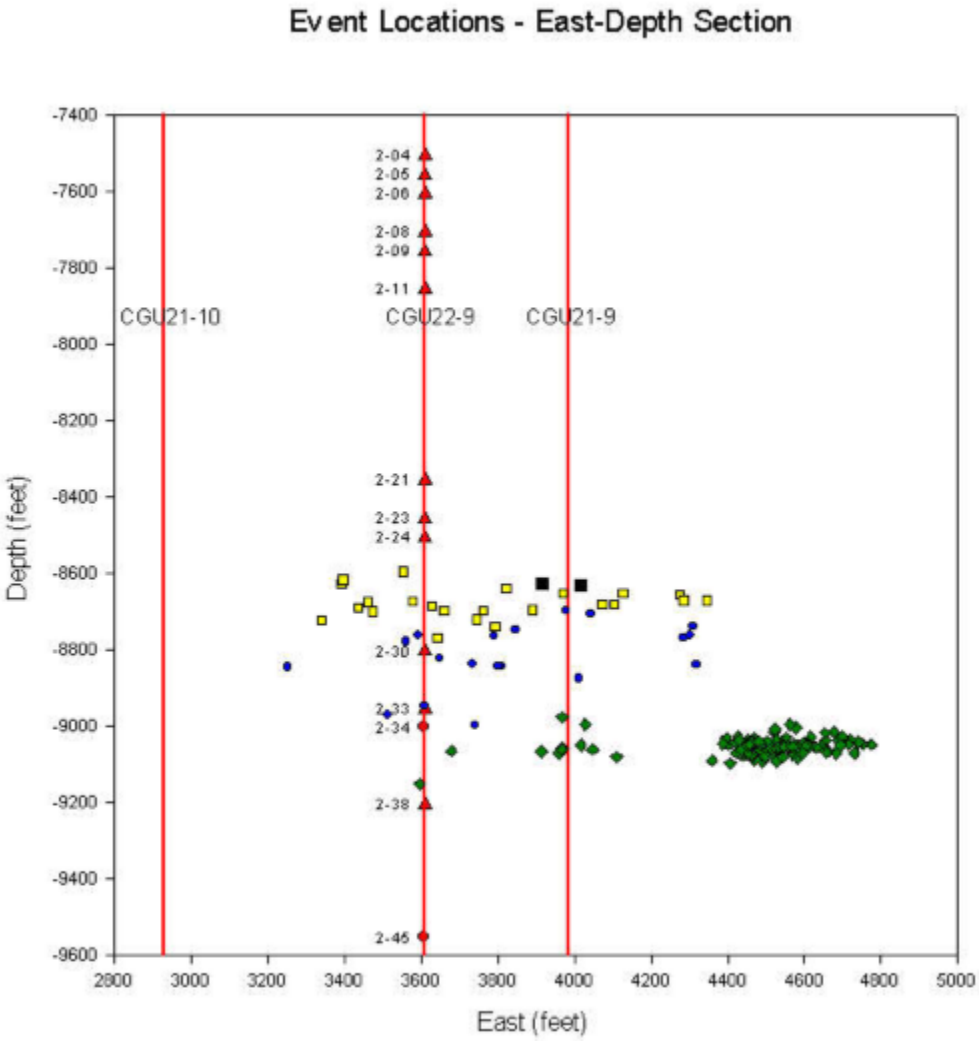

Figure 5. Longitudinal view of the seismicity recorded during Phase II. The monitoring array used in the analysis is as indicated in well CGU22-9.

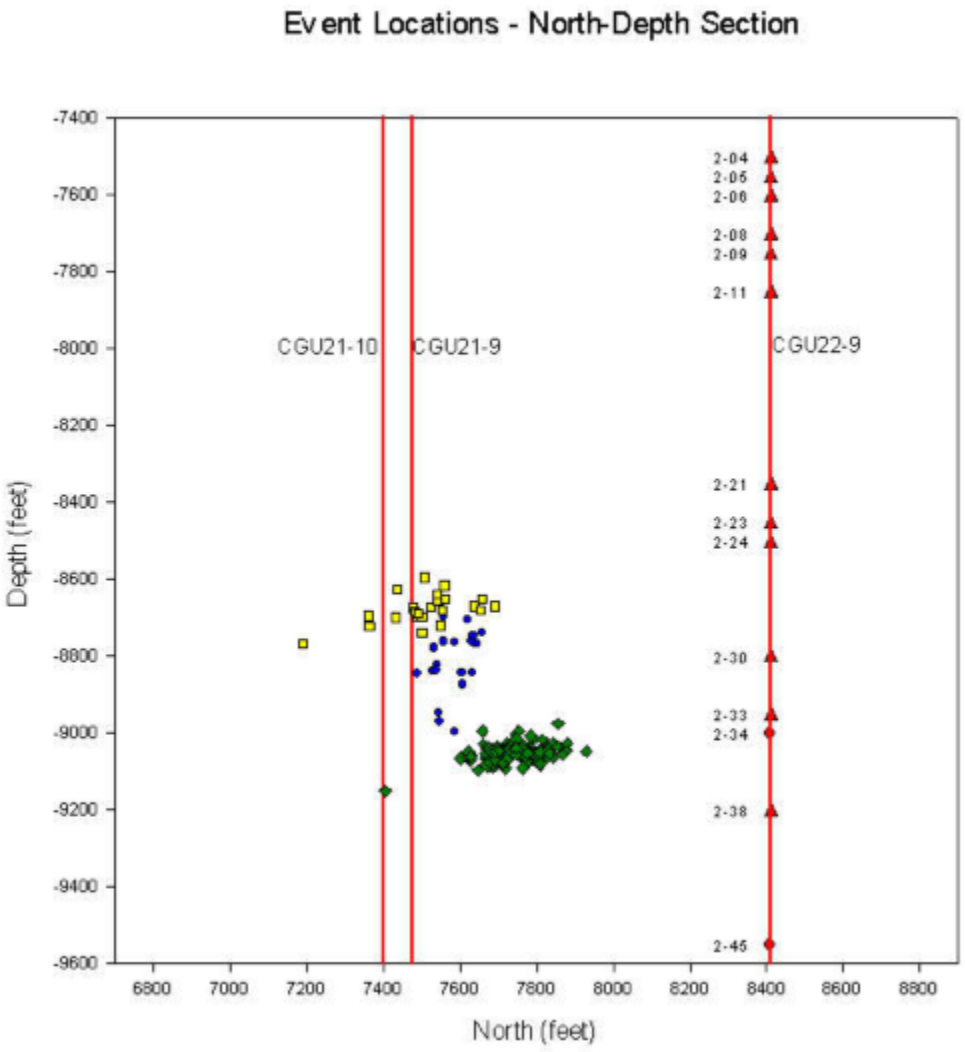

Figure 6. Cross-sectional view of the seismicity recorded during Phase II. The monitoring array used in the analysis is as indicated in well CGU22-9.

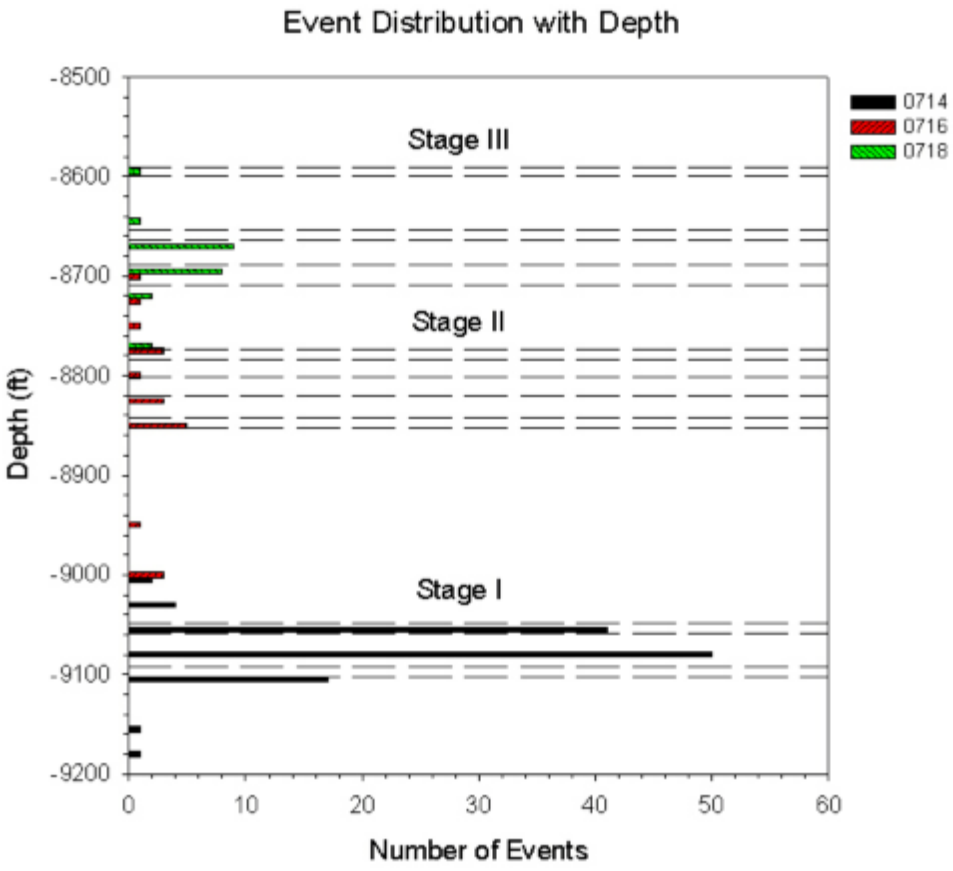

Figure 7. Histogram of event location with respect to depth for the 3 stages of hydraulic fracture during Phase II. Dashed lines bound the perforation depths.

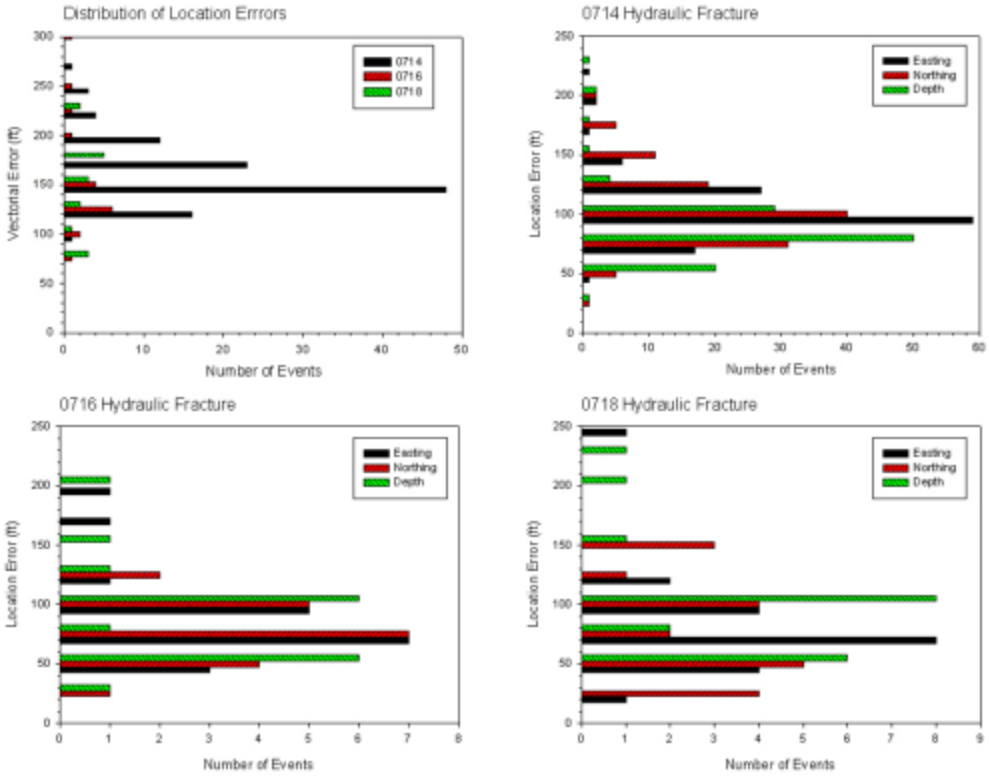

Figure 8. Distribution of event location vectorial errors and by easting, northing, and depth for the 3 fracture stages

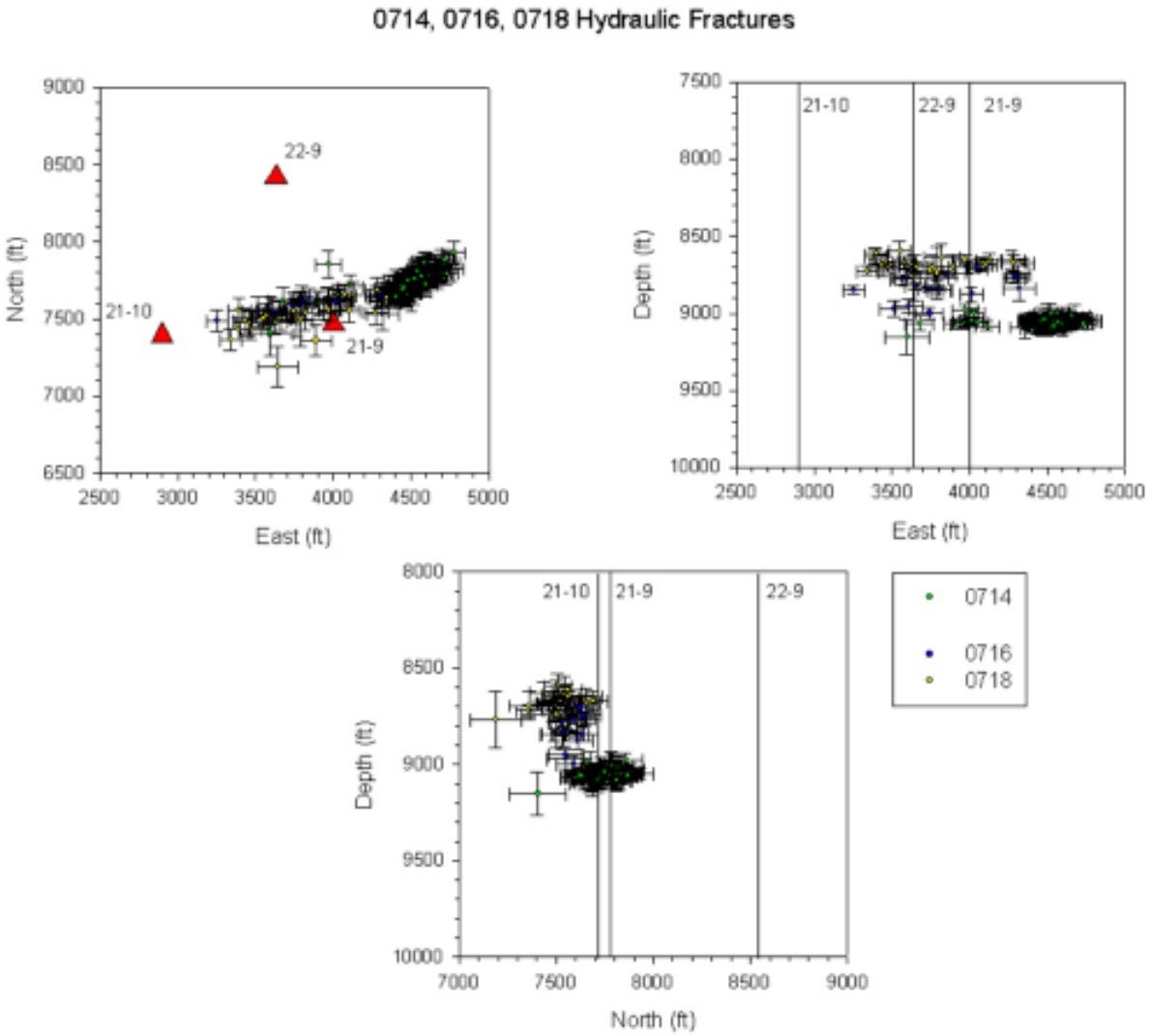

Figure 9. Event locations in plan, longitudinal, and cross-sectional views along with corresponding location errors for the 0714, 0716, and 0718 hydraulic fractures. Bars lengths are scaled with respect to axes.

4.1 7/14/1997 Results

The waveform data from this first stage of the fracture were the highest quality of the three data sets. Figure 10 shows the distribution of microseismic events from this stage in plan view. The earliest events recorded were clustered close to the treatment well. There appears to be an asymmetric distribution of events with most occurring on the eastern limb of the anticipated fracture location, up to 900 feet to the east of the treatment well (only two events were located to the west of the treatment well). Additionally, the majority of events were located within the overall depth bounds of the perforated zone (9010' to 9061'; Figures 11 and 12)).

4.2 7/16/1997 Results

The events from the second stage of hydraulic fracturing are more symmetrically distributed on either side of the treatment well (Figure 13), with events extending about 700 feet to the west and 400 feet to the east of the treatment well. There is somewhat more scatter of event locations in depth for this stage but again, most of the events fall within the limits of the perforations in the treatment well (8736'-8814'), with a few outlying events (Figures 14 and 15). Interestingly, the event distribution appears to be shifted northwards with respect to the anticipated fracture orientation and the event distribution observed for 7/14/1997. It can be speculated that the Phase II hydraulic fracture has been influenced by the presence of the fracture zone created during Phase I, as the event locations appear to continue the trend previously observed (see Urbancic, 1998).

4.3 7/18/1997 Results

The events from the final day of hydraulic fracturing also show a linear trend, extending from about 650 feet to the west of the well and 400 feet to the east of the treatment well (Figure 16). As with the previous days fracture tests, these events are quite well constrained within the limits of the perforation zones (8552'-8671'; Figures 17 and 18). With respect to the 7/16/1997 event distribution, there is a small shift towards the south, however, this difference may be the result of the additional uncertainty resulting from poorer data quality for this particular data set.

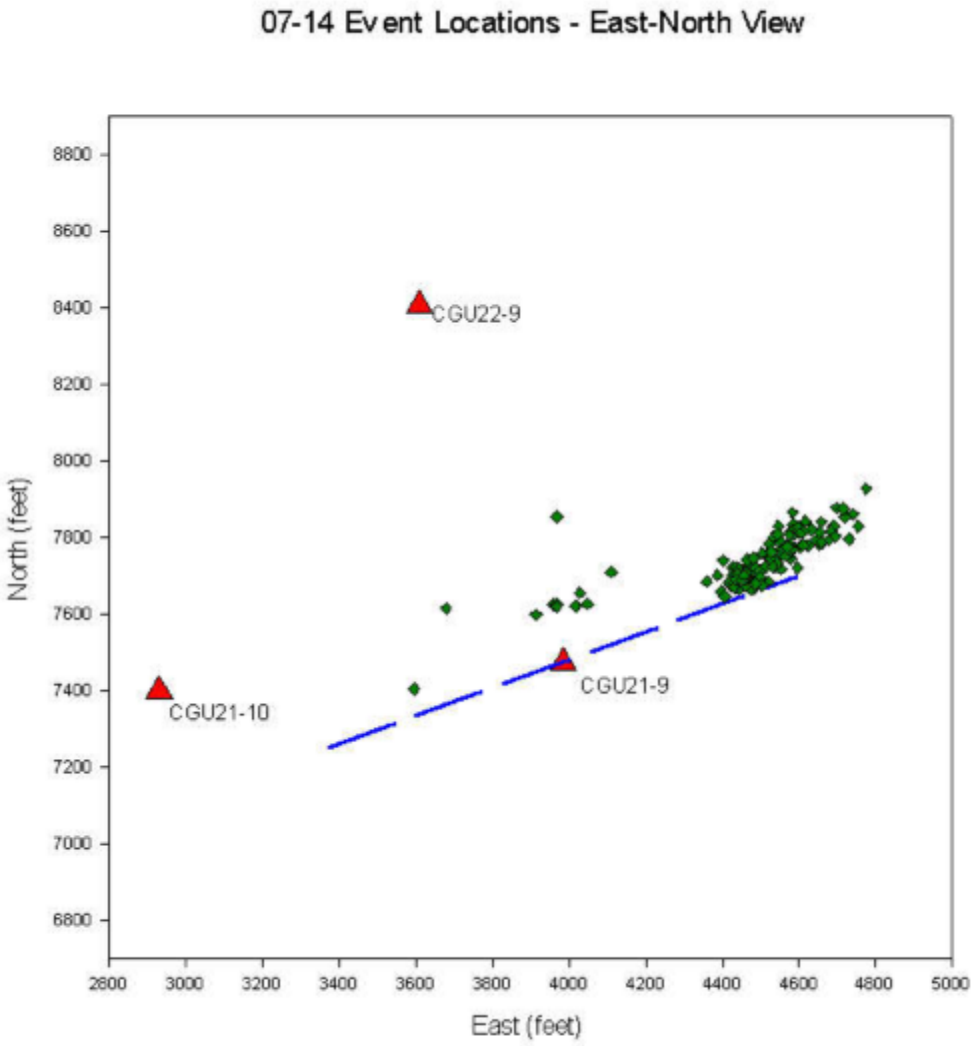

Figure 10. Plan view of event locations obtained for the 0714 hydraulic fracture

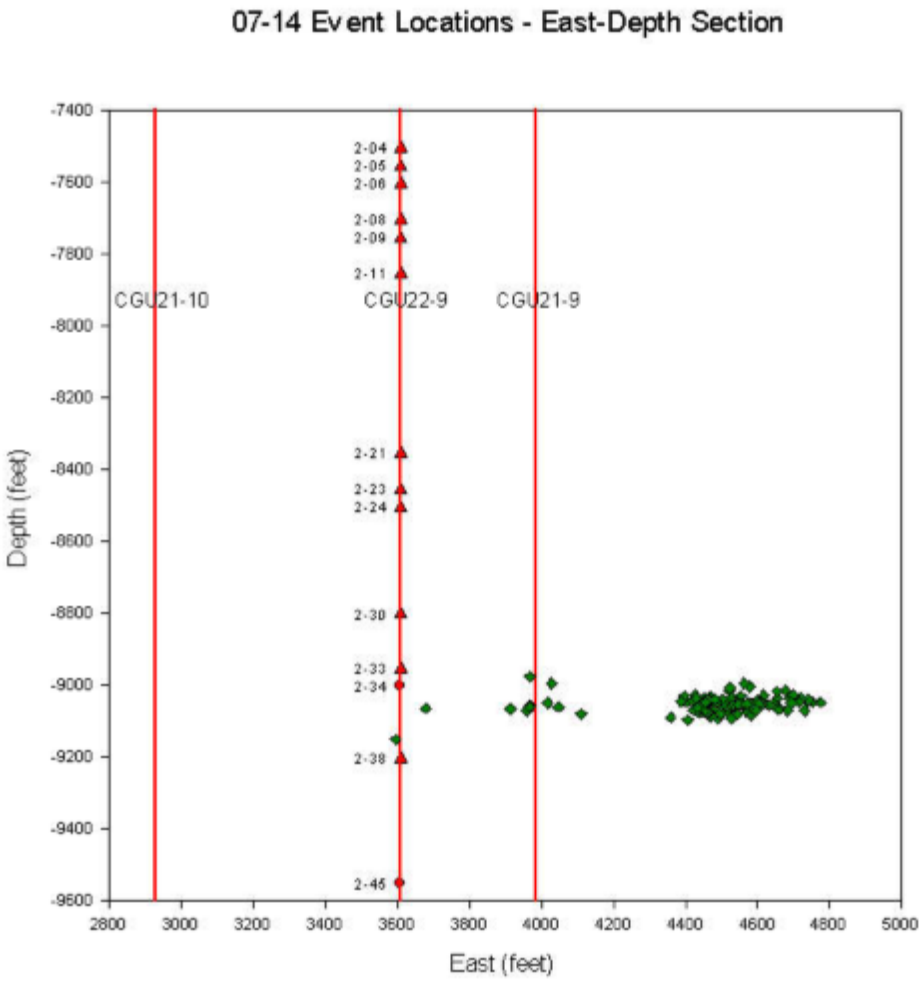

Figure 11. Longitudinal view of event locations obtained for the 0714 hydraulic fracture

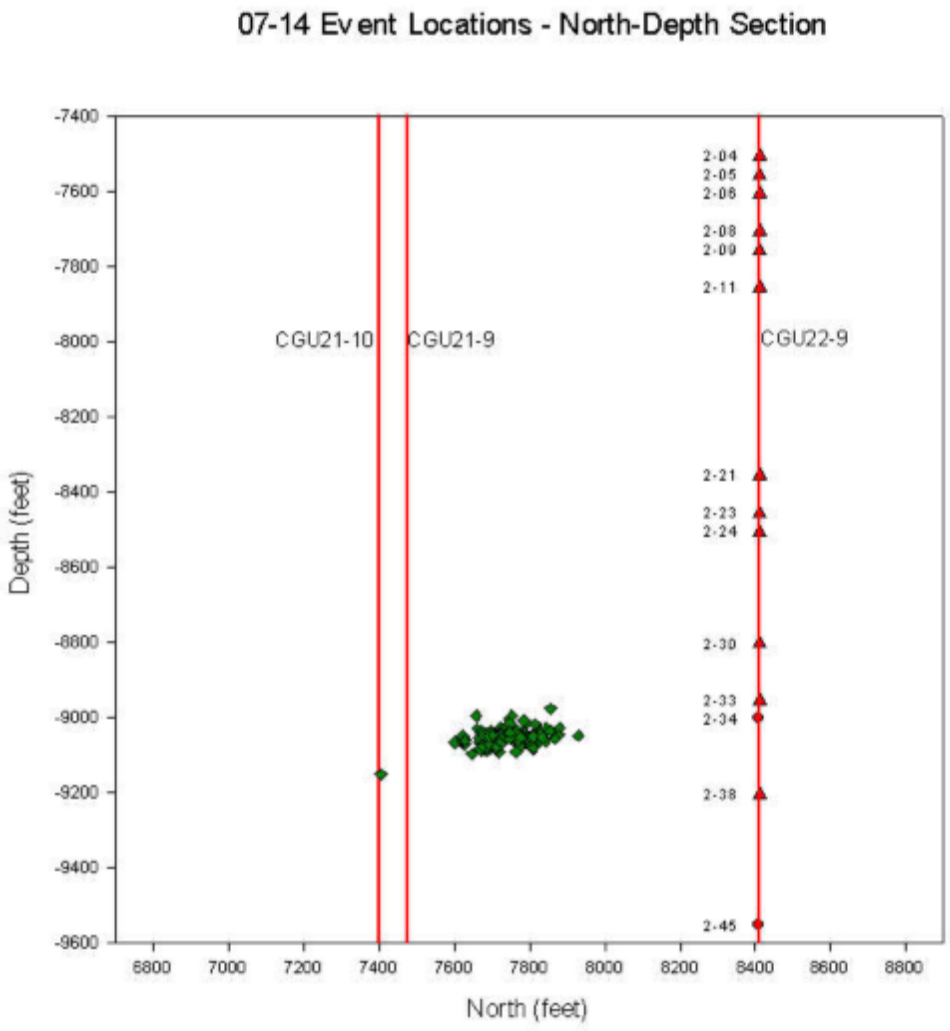

Figure 12. Cross-sectional view of event locations obtained for the 0714 hydraulic fracture

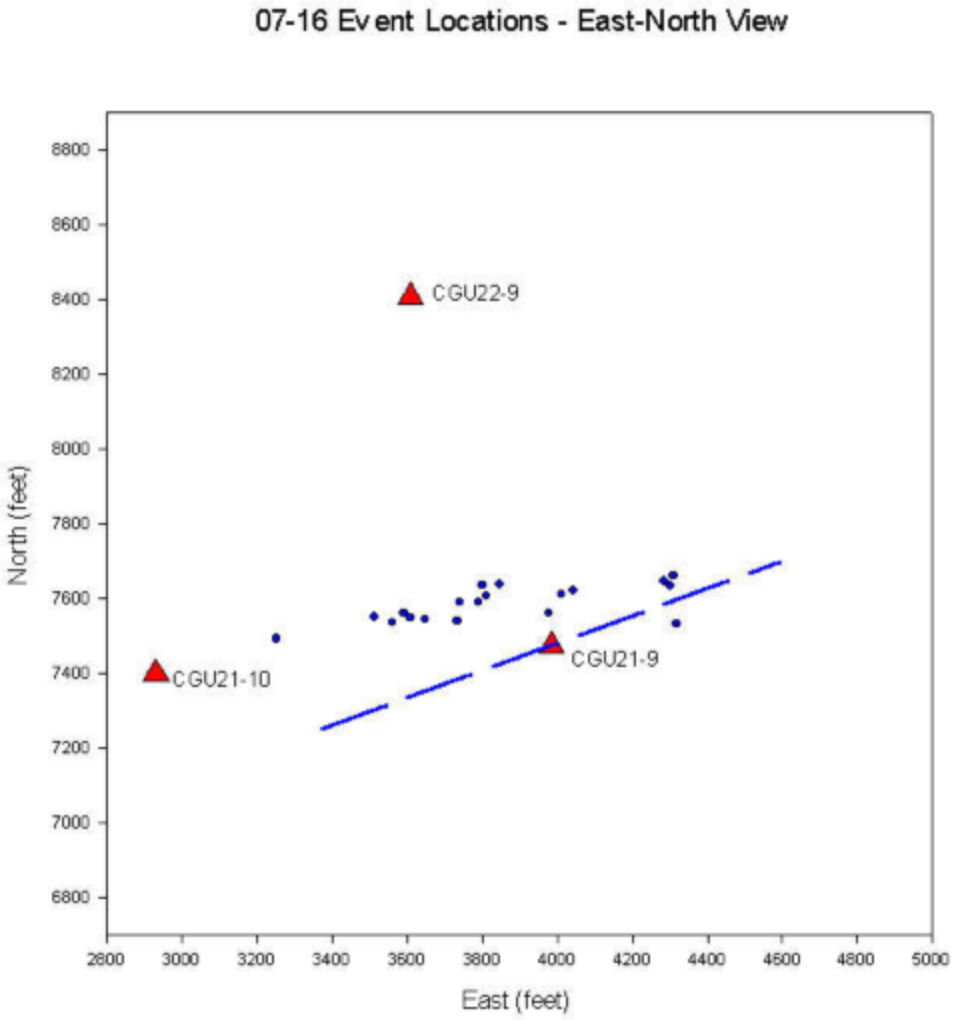

Figure 13. Plan view of event locations obtained for the 0716 hydraulic fracture

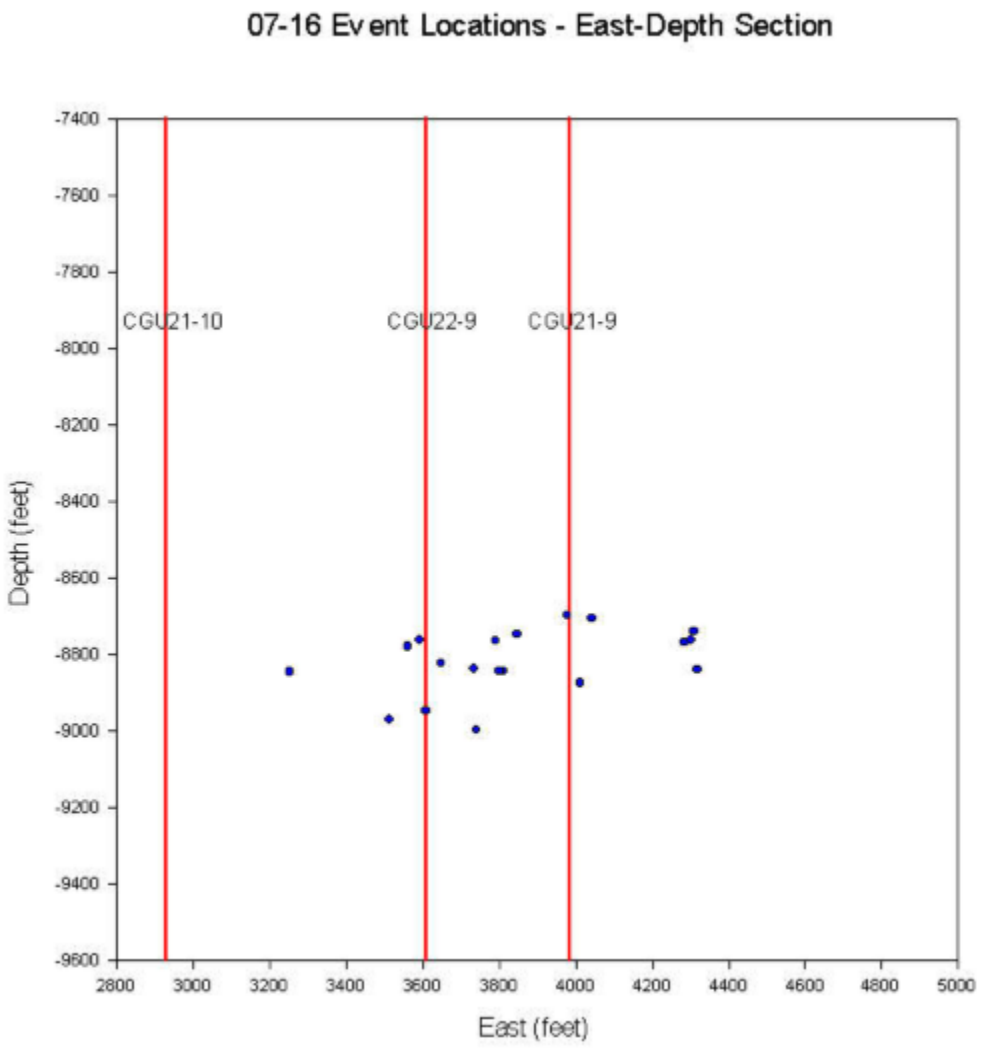

Figure 14. Longitudinal view of event locations obtained for the 0716 hydraulic fracture

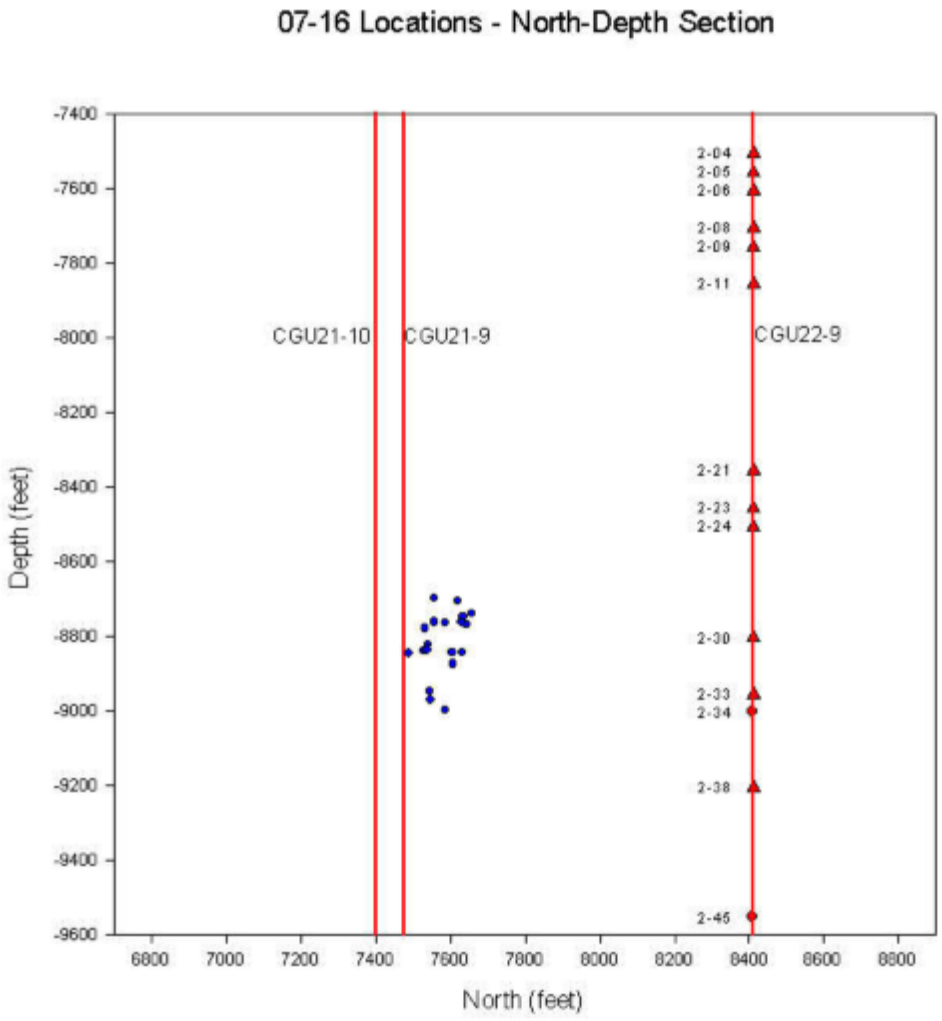

Figure 15. Cross-sectional view of event locations obtained for the 0716 hydraulic fracture

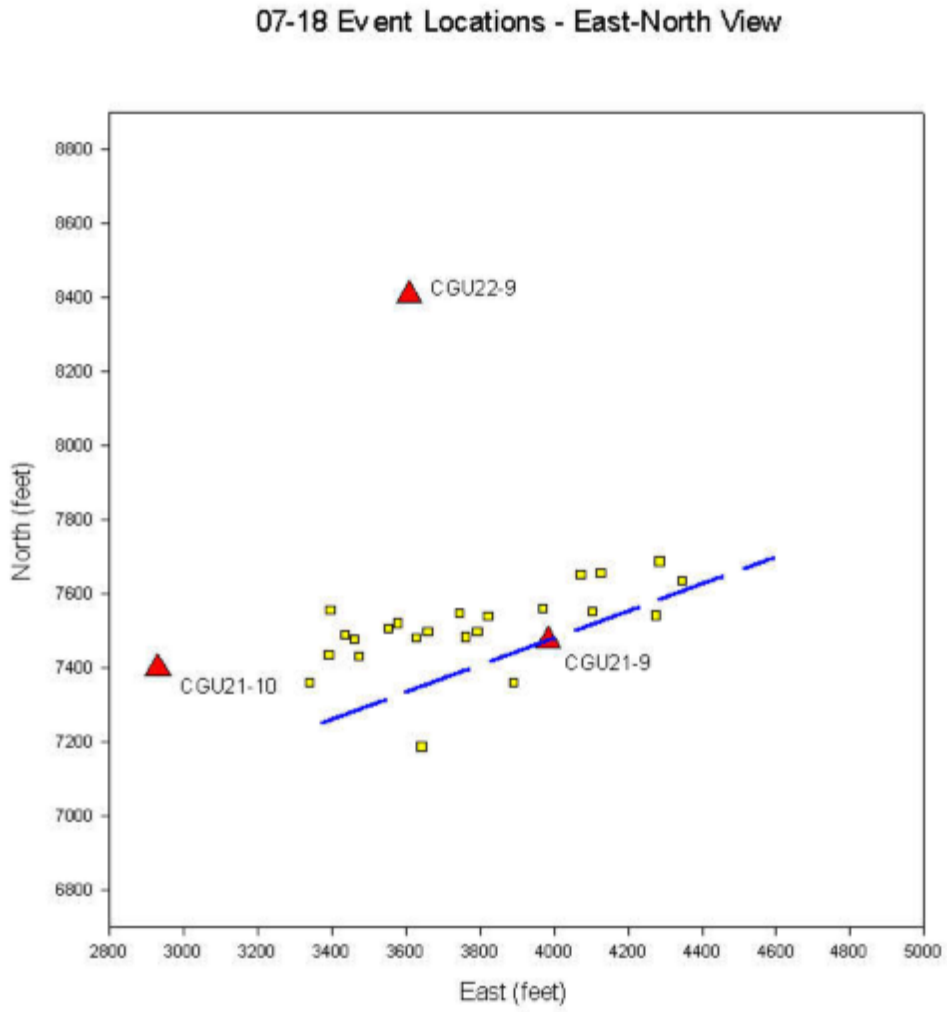

Figure 16. Plan view of event locations obtained for the 0718 hydraulic fracture

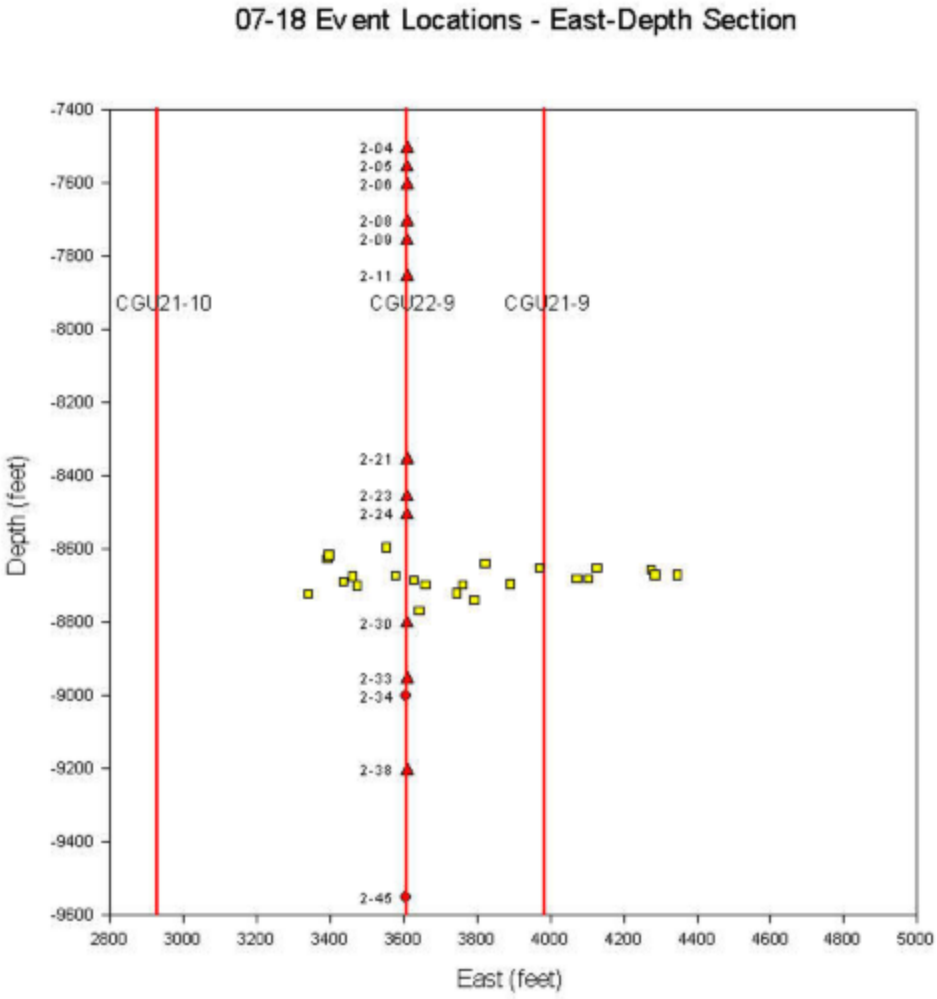

Figure 17. Longitudinal view of event locations obtained for the 0718 hydraulic fracture

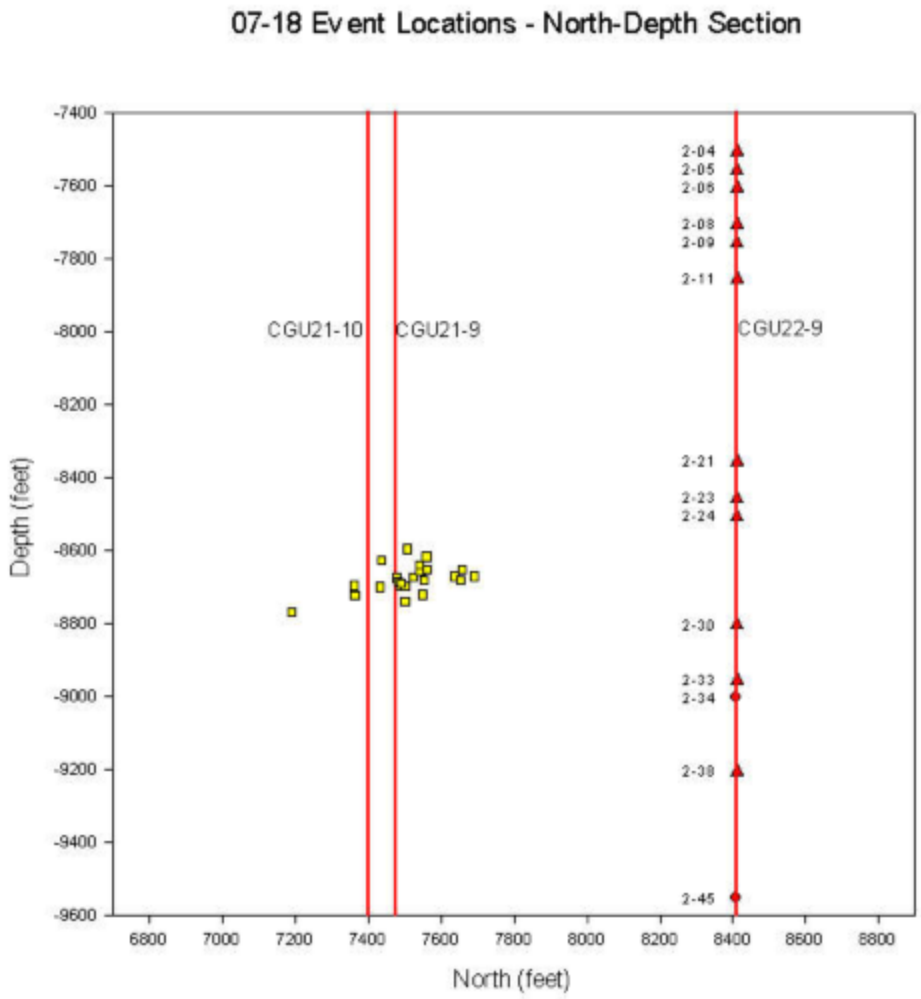

Figure 18. Cross-sectional view of event locations obtained for the 0718 hydraulic fracture

5.0 Conclusions

As outlined in the introduction, the main purpose of this study was to provide an independent assessment of the Phase II data and to re-calculate the event locations reported by Withers and Dart. As part of this analysis, an evaluation of triaxial geophone orientation was made on the basis of hodogram (particle motion diagram) analysis using primacord shots from Phase I and Phase II perforation shots. The azimuths for different shot-sensor combinations varied within 2 to 3 degrees, and were within 18 degrees of the rotoscan derived orientations. Using a two stage inversion scheme, events locations were determined based on single well P- and S-wave arrival times, and both P- and S-wave polarization angles to an accuracy of about +/- 150 ft..

Different from the arced distribution of Withers and Dart, the re-analysis indicates that the events were generally linearly distributed with an orientation of N75°E, similar to the predicted orientation and to the observed trends in Phase I. The events were well constrained in depth, with the majority of the events occurring within the perforation depths. An analysis of the microseismicity for each stage (daily) of the experiment outlined two trends, 1) that there appears to be an asymmetric distribution of events (up to 900 ft. east of the treatment well), and 2) that a northward shift in event locations for the latter stages may be related to the interaction between the current fracture development and the fracture zone established during Phase I.

One of the main obstacles in providing an on-line approach to event location determination is the relatively low P-wave energy observed with respect to S-wave energy present in the signals. As discussed, in many instances the P-wave are lost in the background noise, not allowing for typical P-wave based hodogram analysis to be considered. The S-waves, however, are generally exhibit strong arrivals. The location technique employed incorporated S-wave hodogram evaluations into the analysis. The positive results obtained suggest that this method could be adapted to allow for on-line determination of event locations from single well geometries. It is recommended that this approach be evaluated if a more complete description of the Phase II hydraulic fractures is required and if commercialization is an objective of the current set of investigations.

References

Press W.H., Teukolsky, S.A., Vetterling, W.T., and Flannery, B.P.,1992. Numerical recipes in fortran: The art of scientific computing, Cambridge University Press, 963 p..

Rutledge, J.T., Phillips, W.S., House, L.S., and Zinno, R.J., 1998. Microseismic mapping of a Cotton Valley hydraulic fracture using decimated arrays. Submitted to SEG 1998 meeting, New Orleans, 4 p.

.

Urbancic, T.I., 1998. Cotton Valley Hydraulic Fracture Imaging Project: Feasibility of determining fracture behavior using microseismic event locations and source parameters, Report ESG98-02 to UPR Sponsored Industry Consortium, 35 p..

Walker, R.N., 1997. Cotton Valley Hydraulic Fracture Imaging Project, SPE contribution 38577, 16 p.

Warpinski, N., 1997. A re-analysis of the Cotton Valley Hydraulic Fracture Imaging Project: Imaged geometry of the Taylor Sand Hydraulic Fractures. Report submitted to GRI, December, 1997, 14 p..

Withers, R.J. and Dart, R.P., 1997. Cotton Valley Production Stimulation Hydrofracture: Microseismic monitoring & imaging Phase II (CGU21-9 fracture imaging), UPR sponsored consortium, 62 p..